JACS
JOURNAL OF THE AMERICAN CHEMICAL SOCIETY

Article

pubs.acs.org/JACS

Electronic Properties of Bimetallic Metal–Organic Frameworks (MOFs): Tailoring the Density of Electronic States through MOF Modularity

Ekaterina A. Dolgopolova,[†] Amy J. Brandt,[†] Otega A. Ejegbavwo,[†] Audrey S. Duke,[†] Thathsara D. Maddumapatabandi,[†] Randima P. Galhenage,[†] Bryon W. Larson,[‡] Obadiah G. Reid,[‡,§] Salai C. Ammal,[∥] Andreas Heyden,[∥] Mvs Chandrashekhar,[⊥] Vitalie Stavila,[#] Donna A. Chen,*[,†] and Natalia B. Shustova*[,†]

[†]Department of Chemistry and Biochemistry, [∥]Department of Chemical Engineering, [⊥]Department of Electrical Engineering, University of South Carolina, Columbia, South Carolina 29208, United States

[‡]Chemistry and Nanoscience Center, National Renewable Energy Laboratory, Golden, Colorado 80401, United States

[§]Renewable and Sustainable Energy Institute, University of Colorado at Boulder, Boulder, Colorado 80309, United States

[#]Sandia National Laboratories, Livermore, California 94551, United States

Supporting Information

ABSTRACT: The development of porous well-defined hybrid materials (e.g., metal–organic frameworks or MOFs) will add a new dimension to a wide number of applications ranging from supercapacitors and electrodes to "smart" membranes and thermoelectrics. From this perspective, the understanding and tailoring of the electronic properties of MOFs are key fundamental challenges that could unlock the full potential of these materials. In this work, we focused on the fundamental insights responsible for the electronic properties of three distinct classes of bimetallic systems, $M_{x-y}M'_y$-MOFs, $M_xM'_y$-MOFs, and M_x(ligand-M'_y)-MOFs, in which the second metal (M') incorporation occurs through (i) metal (M) replacement in the framework nodes (type I), (ii) metal node extension (type II), and (iii) metal coordination to the organic ligand (type III), respectively. We employed microwave conductivity, X-ray photoelectron spectroscopy, diffuse reflectance spectroscopy, powder X-ray diffraction, inductively coupled plasma atomic emission spectroscopy, pressed-pellet conductivity, and theoretical modeling to shed light on the key factors responsible for the tunability of MOF electronic structures. Experimental prescreening of MOFs was performed based on changes in the density of electronic states near the Fermi edge, which was used as a starting point for further selection of suitable MOFs. As a result, we demonstrated that the tailoring of MOF electronic properties could be performed as a function of metal node engineering, framework topology, and/or the presence of unsaturated metal sites while preserving framework porosity and structural integrity. These studies unveil the possible pathways for transforming the electronic properties of MOFs from insulating to semiconducting, as well as provide a blueprint for the development of hybrid porous materials with desirable electronic structures.

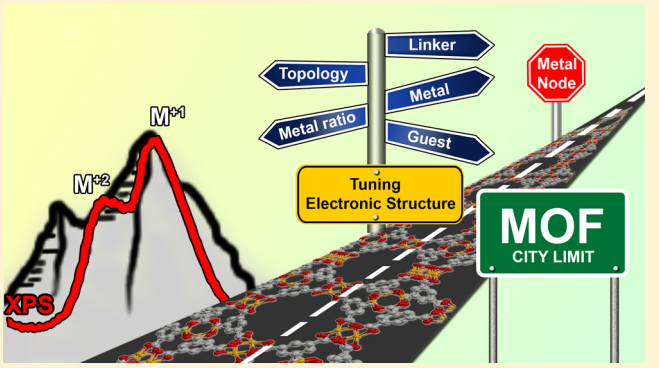

INTRODUCTION

Electronic properties of well-defined metal–organic materials (e.g., metal–organic frameworks or MOFs) have recently become a cutting-edge area of research due to potential transformative effects on the development of semiconductor and supercapacitor technologies, high surface area conductors, thermoelectrics, coatings in electronic engineering, photocatalysts, and sensitive artificial "noses".[1−24] One of the main driving forces for these studies is to complement the intrinsic porosity of MOFs with desirable electronic behavior. The first steps in this direction have clearly demonstrated a very promising start, which includes the development of chemiresistive sensors, crystalline materials with a high charge mobility, and porous electrodes.[11,25−33] However, there are a number of challenges that must be overcome for further successful advancement in this area. One of them is the preparation of conductive hybrid materials that preserve framework crystallinity without blocking MOF pores. Metal node engineering is one of the strategies for the preservation of MOF porosity while tuning MOF electronic structure. As previously shown, a MOF matrix can accommodate a second

Received: February 4, 2017
Published: March 18, 2017

DOI: 10.1021/jacs.7b01125
J. Am. Chem. Soc. XXXX, XXX, XXX−XXX

metal without loss of crystallinity.[34−41] Tailoring of electronic properties could therefore be performed through "guest metal" immobilization inside MOF metal nodes. Thus, the objective of the presented studies is fundamental understanding of key parameters, which may impact the tailoring of electronic structure in bimetallic MOFs through framework modularity.

Very recently, it was shown that the electrical conductivity of MOF samples is affected by many factors including grain boundaries and anisotropy, which hinder screening and comparison of different MOF samples, especially without access to their single crystals.[42] From this perspective, we present a comprehensive approach that allows one to experimentally prescreen the changes in the electronic structures of complex bimetallic systems while simultaneously monitoring changes in metal oxidation states occurring on the metal nodes. These studies can then guide the selection of the most promising candidates for further detailed investigations. In this work, we utilized three distinct types of bimetallic systems shown in Scheme 1: $M_{x-y}M'_y$-MOFs (type I), $M_xM'_y$-MOFs (type II), and M_x(ligand-M'_y)-MOFs (type III). In particular, our approach couples: (i) state-of-the-art surface science techniques to prescreen changes in the density of electronic states (DOS) near the Fermi edge while monitoring changes in the metal oxidation states; (ii) material design including utilization of MOF modularity through incorporation of the second metal into the metal node as well as its coordination to the organic linker; (iii) microwave conductivity measurements to estimate intrinsic conductance of the selected MOF samples; and (iv) theoretical modeling. We attempt to shed light on the fundamental understanding of how metal node composition and geometry and/or MOF topology could affect the electronic structure, thereby establishing a pathway for tuning the conductivity of MOFs that are normally insulating.

Scheme 1. A Schematic Representation of Monometallic and Bimetallic MOFs[a]

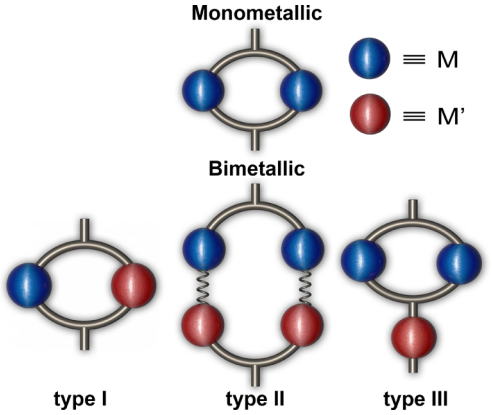

[a]Semiovals with sandwiched metals and grey sticks represent the metal nodes and organic linkers, respectively. Type I $M_{x-y}M_y'$-MOFs: incorporation of M′ occurs through the replacement of M. Type II M_xM_y'-MOFs: M′ incorporation extends metal nodes. Type III M_x(ligand-M'_y)-MOFs: M′ coordinates to an organic linker.

RESULTS AND DISCUSSION

In the presented approach, we utilize a number of advantages offered by the MOF platform including: (i) modularity, which allows us to prepare isostructural monometallic and bimetallic frameworks for detailed understanding and comparison of possible changes in the electronic structure that appear after the incorporation of the second metal; (ii) crystallinity, which permits comprehensive structural analysis of MOF topology and metal node geometry; and (iii) porosity, which provides an opportunity to study the electronic structure as a function of substrate dynamics.

We have applied these advantages to studying the effect of a second metal on the electronic structure of three distinct bimetallic systems shown in Scheme 1 (types I−III). The type-I $M_{x-y}M'_y$-MOFs consists of bimetallic nodes, which are isostructural to monometallic analogues. In this case, the incorporation of the second metal, M′, occurs through the replacement of M, and therefore both M and M′ possess the same coordination environment (Scheme 1, type I). One of the most studied examples of the type-I platform is IRMOF-1.[43−48] Type II of the bimetallic $M_xM'_y$-MOFs also contains bimetallic nodes, but M′ incorporation results in metal node extension instead of M substitution (Scheme 1, type II) and therefore significant changes in the local environment of M′ versus M. An example of such node extension was recently reported by the Zhou group who extended the hexameric Zr-based nodes to decameric $Zr_6M'_4$.[49] Type III M_x(ligand-M'_y)-MOFs consist of monometallic nodes, and M′ coordinates to the organic linker as shown in Scheme 1. One example of M_x(ligand-M'_y)-MOFs was recently prepared by Lin and co-workers through utilization of organic linkers in the Zr-based framework as an anchor for a second metal incorporation.[50]

Our initial studies were focused on type I bimetallic $M_{x-y}M'_y$-MOFs due to a wide range of M/M′ metal pairs already being incorporated into the MOF matrix[40,51−55] and therefore available for systematic studies. The major criterion imposed on the selection of $M_{x-y}M'_y$-MOFs was the possibility of solvent removal with preservation of the framework's structural integrity. This property is crucial for the initial prescreening of MOF electronic properties by X-ray photoelectron spectroscopy (XPS). Our previous investigations[56] of monometallic frameworks demonstrated that mixed-valence metals such as copper could significantly affect the density of states near the Fermi edge. For instance, we observed that presence of Cu^{1+}/Cu^{2+} sites resulted in significant changes in the valence band structure.[56] Consequently, we have focused on $M_{3-y}M'_y(BTC)_2$ (M = Cu, H_3BTC = benzene-1,3,5-tricarboxylic acid) as a first model system for type-I bimetallic MOFs based on potential tunability of the valence band structure through the presence of mixed valence metal sites, as well as required thermal stability (Figure 1). As a Cu (M) counterpart, we have chosen Co and Zn for three main reasons. The first reason is that the introduction of both Zn and Co inside the Cu-MOF could be performed by a relatively straightforward synthetic approach, which resulted in bimetallic systems isostructural to monometallic analogues. This also allowed us to prepare bimetallic MOFs with a different M/M′ ratio and study the electronic properties as a function of the metal ratio. Second, these metals will allow us to test the effect on electronic structure of divalent zinc versus cobalt, which could exhibit +2 and +3 oxidation states. Finally, recent theoretical studies focusing on electronic structure elucidation of bimetallic systems suggest that Co-incorporation into IRMOF-1 could result in appearance of metallic behavior in the insulating zinc-based MOF.[44]

Solid-state metathesis was chosen as a synthetic method for preparation of bimetallic MOFs with different M/M′ ratios (M = Cu, M′ = Co, Zn). For preparation of $Cu_{3-y}Co_y(BTC)_2$, freshly synthesized $Cu_3(BTC)_2$ was introduced into *N,N*′-

DOI: 10.1021/jacs.7b01125
J. Am. Chem. Soc. XXXX, XXX, XXX−XXX

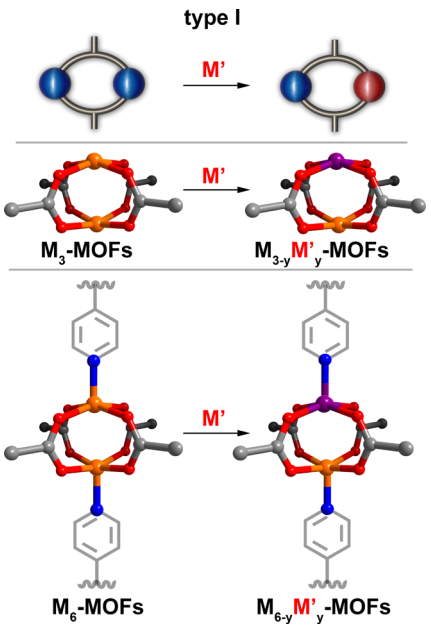

Figure 1. Paddle-wheel metal nodes of $M_{3-y}M'_y$-MOFs with unsaturated metal sites (middle) and $M_{6-y}M'_y(BTB)_4(BP)_3$ with metal sites blocked by the BP ligand. Only one phenyl ring of the BP ligand is shown (bottom). The gray, red, orange, and purples spheres in the metal nodes represent carbon, oxygen, M, and M′, respectively.

dimethylformamide (DMF) solutions with different $CoCl_2$ concentrations, which were heated at 90 °C for 24 h. The $Cu_{3-y}Zn_y(BTC)_2$ samples were prepared by soaking $Zn_3(BTC)_2$ in a saturated solution of $Cu(NO_3)_2$ for 9−18 h at room temperature.[40] Each sample of prepared bimetallic $M_{3-y}M'_y$-MOFs was characterized by powder X-ray diffraction (PXRD), Fourier transform infrared spectroscopy, and thermogravimetric analysis, and the M/M′ ratio was determined by inductively coupled plasma atomic emission spectroscopy. As a result, the following compositions for type I BTC-containing MOFs were studied: $Cu_{3-y}Zn_y(BTC)_2$ (y = 0.75 and 1.05) and $Cu_{3-y}Co_y(BTC)_2$ (y = 0.18, 0.60, and 1.5). The prepared BTC-containing bimetallic MOFs are isostructural to monometallic $M_3(BTC)_2$ (M = Cu and Zn, Figures S1−S7). The $Cu_{3-y}Co_y(BTC)_2$ and $Cu_{3-y}Zn_y(BTC)_2$ samples were evacuated at 120−150 °C (48 h) and at 100−160 °C (48 h) on the Schlenk line, respectively, before the XPS studies. In addition, some MOF samples were pretreated by heating at 100−225 °C in a specialized cell under an argon atmosphere before introduction into the XPS chamber. PXRD was used for confirmation of framework crystallinity after evacuation and additional heating in the inert atmosphere. More detailed procedures used for each set of samples are given in Table 1 (vide infra).

XPS valence band spectra provide information about the electronic properties of the MOFs since the signal intensities reflect the densities of states near the Fermi level (E_F, binding energy =0 eV). As shown in Figure 2, the valence band spectra of the evacuated monometallic M-MOFs (M = Cu and Zn) and bimetallic $M_{3-y}M'_y$-MOFs (M = Cu, M′ = Zn) exhibit zero intensity near the Fermi level, and this absence of electronic states around E_F is characteristic of insulators. Furthermore, there is a distinct change in the DOS for $Cu_3(BTC)_2$ after heating under an argon atmosphere at 225 °C, given that the valence band spectrum shows a significant increase in intensity

Table 1. Thermal Treatment Procedures for Prepared Monometallic and Bimetallic MOFs

MOF systems	evacuation procedure temp., time	additional thermal treatment[a]
$Cu_3(BTC)_2$	160 °C, 48 h	225 °C, 14 h
$Zn_3(BTC)_2$	100 °C, 24 h	100 °C, 4 h
$Cu_3(BTB)_2$	100 °C, 4 h	100 °C, 1 h
$Cu_6(BTB)_4(BP)_3$	100 °C, 24 h	
$Co_6(BTB)_4(BP)_3$	130 °C, 6 h	
$Co_6(BTC)_2(HCO_2)_6(DMF)_6$	100 °C, 8 h	
$Zn_{0.75}Cu_{2.25}(BTC)_2$	160 °C, 48 h	130 °C, 4 h
$Zn_{1.05}Cu_{1.95}(BTC)_2$	160 °C, 48 h	225 °C, 14 h
$Cu_{2.82}Co_{0.18}(BTC)_2$	160 °C, 48 h	225 °C, 14 h
$Cu_{2.4}Co_{0.6}(BTC)_2$	120 °C, 48 h	
$Co_{1.5}Cu_{1.5}(BTC)_2$	120 °C, 48 h	160 °C, 14 h
$Cu_{2.34}Co_{3.66}(BTB)_4(BP)_3$	130 °C, 24 h	
Zr_6Co_4-MOF	rt[b], 1 h	
$Zr_6O_4(OH)_4$(sal-TPD-Co)	rt, 2 h	
Zr_6-MOF	rt, 1 h	
$Zr_6O_4(OH)_4$(sal-TPD)	rt, 2 h	

[a]Additional treatment was performed in the specialized cell under an argon atmosphere before sample transfer into the XPS chamber. [b]rt = room temperature.

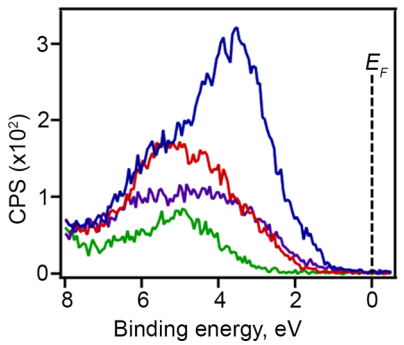

Figure 2. XPS data for the valence band region for: $Cu_3(BTC)_2$ (red), $Cu_3(BTC)_2$ (additional heating at 225 °C for 14 h under argon, blue), $Zn_3(BTC)_2$ (green), and $Cu_{2.25}Zn_{0.75}(BTC)_2$ (purple). A sample treatment is given in Table 1.

at the Fermi edge after heating. In our previous work, we have attributed this change in electronic structure to the coexistence of mixed valence Cu^{1+} and Cu^{2+} sites.[56]

While the pure $Cu_3(BTC)_2$ sample contains mixed valence sites, the zinc-based analogue $Zn_3(BTC)_2$ exhibits a single $Zn(2p_{3/2})$ peak at 1022.4 eV, which is consistent with the metal nodes in only the +2 oxidation state.[57,58] Similarly, for bimetallic $Cu_{3-y}Zn_y$-MOFs, Cu is found in both the +1 and +2 oxidation states, whereas Zn exists exclusively as +2 (Figure S8). The assignment of the Cu^{1+} and Cu^{2+} oxidation states are based on both the $Cu(2p_{3/2})$ and Cu(LMM) regions; these assignments are discussed in the Supporting Information (SI) section and have also been described in detail in a previous manuscript.[56] Moreover, heating the bimetallic sample containing 35% zinc ($Cu_{1.95}Zn_{1.05}(BTC)_2$) to 215 °C for 14 h under an argon atmosphere resulted in an increase in the Cu^{1+} intensity and an increase in DOS near the valence band edge (Figure S9). Thus, the presence of Zn^{2+} does not prevent the reduction of Cu^{2+} to Cu^{1+} or prevent changes in the valence band spectrum after MOF heating.

DOI: 10.1021/jacs.7b01125
J. Am. Chem. Soc. XXXX, XXX, XXX−XXX

In contrast to zinc-incorporated frameworks, we have observed significant differences in the electronic structure for the series of cobalt-substituted bimetallic MOFs. Specifically, the XPS valence band region for $Cu_{3-y}Co_y(BTC)_2$ samples (y = 0.18 and 1.5) show nonzero intensity near E_F, demonstrating that electronic states exist in this region, and a cobalt content of only 6% (y = 0.18) is sufficient to facilitate this change (Figure S10). As mentioned above, the appearance of electronic states near E_F in the valence band spectrum is behavior characteristic of semiconductors. As a control experiment, we also investigated the valence band region of the $CoCl_2$ salt used for the preparation of bimetallic frameworks. As expected, DOS for $CoCl_2$ near E_F is zero, unlike what is observed for $Cu_{3-y}Co_y$-MOFs (Figure S11).

In terms of the oxidation of the metals, the $Cu_{3-y}Co_y(BTC)_2$ (y = 0.18 and 1.5) samples exhibit both Cu^{1+} and Cu^{2+} oxidation states (Figure S10). For the $Cu_{3-y}Co_y(BTC)_2$ MOFs, the Co(2p) region is consistent with Co^{2+}, based on the presence of strong satellite features, the splitting of the $2p_{3/2}$ and $2p_{1/2}$ peaks, and the Co($2p_{3/2}$) binding energy (see Supporting Information for more details). Similar to bimetallic $Cu_{3-y}Zn_y(BTC)_2$, heating of $Cu_{3-y}Co_y(BTC)_2$ induces the reduction of Cu^{2+} to Cu^{1+}, and therefore the presence of cobalt in the MOF structure does not prevent Cu^{2+} reduction.

Since there are no synthetic reports of a pure $Co_3(BTC)_2$ phase isostructural to bimetallic $Cu_{3-y}Co_y(BTC)_2$, we attempted to analyze a different Co-BTC-containing phase consisting of hexanuclear metal nodes connected by BTC^{3-} linkers (Figures S12 and S13).[59] However, the loss of MOF structural integrity was observed. XPS measurements performed on the degraded sample did not reveal any similarities with the electronic structure of $Cu_{3-y}Co_y$-MOFs. To better understand the unique electronic structure of $Cu_{3-y}Co_y(BTC)_2$, we prepared a $M_6(BTB)_4(BP)_3$ (H_3BTB = benzene-1,3,5-tribenzoate, BP = 4,4′-bipridyl) series, which consists of paddle-wheel metal nodes similar to $M_{3-y}M_y'(BTC)_2$, and integration of the second metal without loss of framework integrity was achieved (Figures S14–S18). Notably, attempts to prepare bimetallic $Cu_{3-y}M_y'(BTB)_2$ without the presence of the second BP linker were not successful despite the existing straightforward synthetic procedure for isostructural monometallic $Cu_3(BTB)_2$. The latter was successfully prepared, and valence spectra showed no electronic states near E_F (Figure S19). However, for the BTB-containing systems, we were able to prepare isostructural monometallic $Co_6(BTB)_4(BP)_3$ by heating $Co(NO_3)_2{\cdot}6H_2O$ in the presence of H_3BTB and BP at 100 °C for 4 days.[60] The $Cu_{6-y}Co_y(BTB)_4(BP)_3$ system was prepared by direct synthesis through heating of cobalt and copper nitrates in the presence of H_3BTB and BP linkers at 100 °C for 96 h. Surprisingly, the valence band spectra demonstrate that electronic properties of $Cu_{2.34}Co_{3.66}(BTB)_4(BP)_3$ are unlike $Cu_{3-y}Co_y(BTC)_2$ but instead are closer to those observed for insulating $Zn_3(BTC)_2$ or $Zn_{3-y}Cu_y(BTC)_2$ (Figure 3). Monometallic $Cu_3(BTB)_2$ (without BP) contains Cu^{1+}/Cu^{2+} metal sites and exhibits DOS like that of the $Cu_3(BTC)_2$ (Figure S19). Electronic properties resembling $Cu_3(BTC)_2$ were also observed for monometallic $Co_6(BTB)_4(BP)_3$. Therefore, MOF topology and/or presence of unsaturated metal sites result in different DOS near E_F for $M_{3-y}M_y'(BTC)_2$ versus $M_{3-y}M_y'(BTB)_2$ despite the similar metal node geometries. To summarize, the $Cu_{3-y}Co_y(BTC)_2$ system possesses an electronic structure like that of a semiconductor near E_F, while the lack of DOS around E_F for $Cu_3(BTC)_2$, $Zn_3(BTC)_2$, $Cu_{3-y}Zn_y(BTC)_2$, $Cu_3(BTB)_2$, and $Cu_{6-y}Co_y(BTB)_4(BP)_3$ is characteristic of insulators.

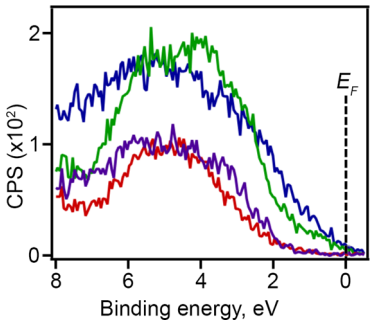

Figure 3. XPS data for the valence band region of $Cu_{1.05}Zn_{1.95}(BTC)_2$ (red), $Cu_{1.5}Co_{1.5}(BTC)_2$ (blue), $Cu_{2.82}Co_{0.18}(BTC)_2$ (green), and $Cu_{2.34}Co_{3.66}(BTB)_4(BP)_3$ (purple). A sample treatment is given in Table 1.

To shed light on the changes of the electronic structure near E_F observed by XPS for bimetallic $Cu_{3-y}Co_y(BTC)_2$, we have performed conductivity measurements on the MOF pressed pellets and microwave conductivity experiments on MOF powders, as well as employed diffuse reflectance spectroscopic studies in combination with theoretical calculations. As a starting point, we measured bulk conductivity on the pressed pellets prepared from evacuated bimetallic $Cu_{2.4}Co_{0.6}(BTC)_2$ and monometallic $Cu_3(BTC)_2$, for which the conductivities were found to be 1.4×10^{-8} S/cm and 2.0×10^{-10} S/cm, respectively. Thus, the observed values for Cu_yCo_{3-y}-MOF conductivity are about 2 orders of magnitude higher in comparison with monometallic isostructural $Cu_3(BTC)_2$, which is in line with the higher DOS at E_F for $Cu_{3-y}Co_y(BTC)_2$ shown by the XPS studies.

Since we expected that bulk conductivity would be greatly affected by factors such as grain boundary resistances and/or by highly randomized orientation of individual grains within a MOF pellet,[42] we performed microwave absorption measurements on Cu_yCo_{3-y}-MOF powders to estimate intrinsic conductivity. The main advantage of this technique is a quantitative measure of the effective conductivity of a sample without the need to fabricate a device, deposit contacts of any kind, or even prepare compact films. Instead, a sample powder can be mounted on a substrate (in our case—quartz) and be positioned within a characterized microwave cavity to maximize interaction with the field, thus providing a high degree of sensitivity to changes in the sample composition and properties. We have measured the change in cavity characteristics as a function of each MOF sample, and we use finite-element calculations to quantify the sample properties from these observations. Figure S20 shows the measured resonance curves for $Cu_{2.4}Co_{0.6}(BTC)_2$ with baseline measurements of the substrate and mounting tape, as well as the moisture dependence of $Cu_3(BTC)_2$. Each resonance is characterized by its position, width, and depth, which jointly encode the change in sample properties from one resonance to the next. By measuring the change in these parameters between an empty cavity, the cavity with a quartz substrate, with a quartz substrate with double-sided mounting tape, and the substrate/tape/MOF powder, we have determined the effective conductivity of each component of the total sample. Similar contactless microwave absorption measurements have been used to estimate the photoconductivity of other MOFs after laser excitation.[25,61−63] Since photoinduced charge generation processes are not yet

DOI: 10.1021/jacs.7b01125
J. Am. Chem. Soc. XXXX, XXX, XXX−XXX

well-understood for MOFs, we have measured the "dark" effective conductivity for $Cu_3(BTC)_2$ and $Cu_{2.4}Co_{0.6}(BTC)_2$ by combining microwave absorption data with electromagnetic simulations of the cavity response. As mentioned above, each sample was mounted in a microwave cavity, and the reflection coefficient of the cavity was measured as a function of frequency about its resonance; the characteristics of the resonance curve are used to calculate the effective conductivity of each material (full experimental details can be found the Experimental Section and Supporting Information). Under a dry nitrogen atmosphere, the effective conductivities were 0.1×10^{-4} S/cm for $Cu_3(BTC)_2$ compared to 3.5×10^{-4} S/cm for $Cu_{2.4}Co_{0.6}(BTC)_2$, which is consistent with the XPS results. Interestingly for $Cu_3(BTC)_2$, the effective conductivity increases upon exposure to moisture in air to 4.3×10^{-4} S/cm after 1 h and eventually to 5.8×10^{-4} S/cm after several hours, accompanied by a color change from deep royal blue to light blue (Figure S21). We use the term effective conductivity here since this measurement is sensitive to both dielectric contributions (i.e., rotating dipoles or solvent molecules) and intrinsic electrical conductivity. Therefore, the observed increase in measured effective conductivity in the $Cu_3(BTC)_2$ after exposure to moisture is likely due to dielectric interactions of water molecules in the framework with the microwaves and may suggest that the 0.1×10^{-4} S/cm value reported here is a conservative upper estimate of the true intrinsic conductivity, further supporting a drastic increase in conductivity going from the monometallic to bimetallic framework.

To rationalize the changes observed in the valence band region of the $Cu_{3-y}Co_y(BTC)_2$ system, we have carried out theoretical calculations on the truncated model of a bimetallic MOF, $MM'(BTC)_4$. The optimized structure of $Cu_2(BTC)_4$ and $CuCo(BTC)_4$ are shown in Figure S22. Density functional theory (DFT) calculations reveal that the substitution of copper with cobalt in $Cu_2(BTC)_4$ results in changes in the electronic structure near E_F. The energy of the highest occupied molecular orbital (HOMO) increases from −7.78 eV to −7.22 eV, and the lowest unoccupied molecular orbital (LUMO) energy decreases from −3.89 eV to −3.99 eV due to the replacement of copper by cobalt. These results are further supported by DOS calculations (Figure 4), which predicted a wide band gap of 3.8 eV for the $Cu_2(BTC)_4$ structure, which is consistent with insulator properties of this material. The partial DOS shown in Figure 4 were obtained by adding up the atomic projected DOS over different groups of elements such as Cu, Co, and O. Although these plots include contribution from all orbitals, the orbital-projected DOS suggest that the partial DOS near E_F originate mainly from the oxygen p-orbitals, whereas DOS above E_F (conduction band) are composed of copper d-orbitals. When copper is substituted with cobalt, the DOS near E_F are dominated by contributions from cobalt d-orbitals, and the band gap is reduced to 3.2 eV. These results suggest that the electronic structure of the copper-based framework can be tuned by metal substitution in the metal nodes, and higher conductivity should be achieved through cobalt incorporation into the Cu-BTC matrix. For an experimental estimation of optical band gaps in both monometallic $Cu_3(BTC)_2$ and bimetallic $Cu_{3-y}Co_y(BTC)_2$, we utilized diffuse reflectance spectroscopy. For better correlation with theoretical values, we have prepared a sample in which 50% of Cu^{2+} (y = 1.5) was substituted by Co^{2+}. The optical band gap values in the $Cu_3(BTC)_2$ and $Cu_{1.5}Co_{1.5}(BTC)_2$ for allowed direct transitions were derived from the Tauc plot by extrapolation of the straight line to the photon energy axis.[64,65] As a result, band gap values of 3.7 and 3.8 eV were roughly estimated for $Cu_{1.5}Co_{1.5}(BTC)_2$ and $Cu_3(BTC)_2$, respectively (Figure S23). The small decrease of the optical band gap in case of the bimetallic cobalt-containing MOF calculated is consistent with the theoretically predicted decreased band gap.

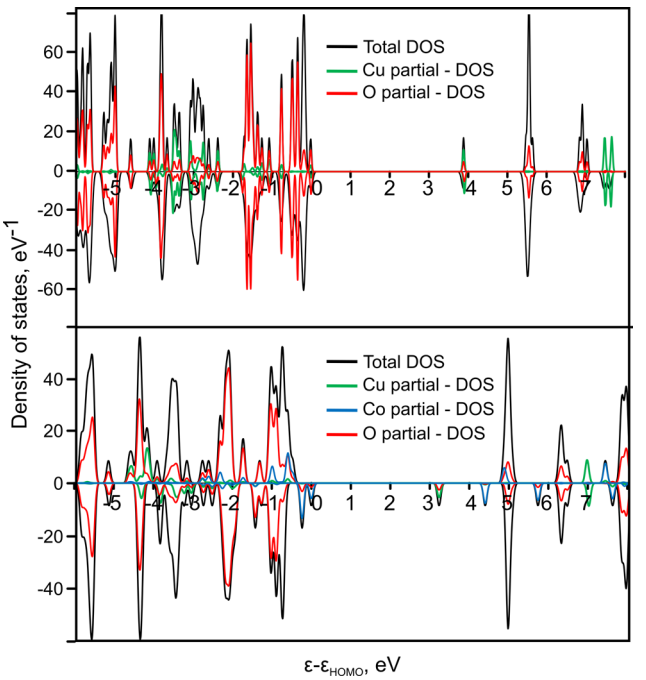

Figure 4. Total and partial density of states (DOS) of: (a) $Cu_2(BTC)_4$ and (b) $CuCo(BTC)_4$ truncated models computed using the B3LYP-D3//def2-TZVPP level of theory.

To gain further insights on the significant changes observed in DOS of type I Cu_yCo_{3-y}-MOFs, we have studied the type II and III bimetallic systems also containing cobalt (Figure 5). For

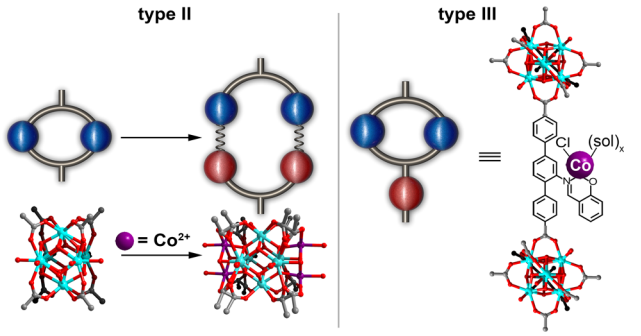

Figure 5. (left) Metal nodes $Zr_6O_4(OH)_8$ extended by the incorporation of Co^{2+} to $Zr_6Co_4O_8(OH)_8$. Turquoise, purple, red, and gray spheres represent zirconium, cobalt, oxygen, and carbon, respectively. (right) Coordination of the second metal, cobalt, occurs through coordination to the organic linker, H_2sal-TPD, instead of the Zr-based metal node.

the preparation of type II bimetallic MOFs, we utilized the approach reported by Zhou and co-workers,[49] in which the Zr-based metal nodes, $Zr_6O_4(OH)_8$, were extended through cobalt incorporation to $Zr_6Co_4O_8(OH)_8$ (Figure 5). For synthesis of Zr_6Co_4-MOF, the prepared Zr-based MOF (PCN-700) was heated in the presence of $Co(NO_3)_2$ salt at 85 °C for 48 h

DOI: 10.1021/jacs.7b01125
J. Am. Chem. Soc. XXXX, XXX, XXX−XXX

(Figure S24).[49] The excess of $Co(NO_3)_2$ was removed by thoroughly washing with DMF.

For the type III MOFs, cobalt was coordinated to the organic linker (Figure 5) using the approach reported by Lin and co-workers.[50] The prepared salicyladimine-based linker (H_2sal-TPD, TPD = terphenyldicarboxylic acid) was heated in the presence of $ZrCl_4$, which resulted in the formation of monometallic $Zr_6O_4(OH)_4$(sal-TPD)$_6$.[50] The coordination of the second metal (Co) was performed by stirring of $Zr_6O_4(OH)_4$(sal-TPD)$_6$ in a solution of $CoCl_2$ in DMF for 24 h at room temperature (Figure S25). Despite both systems containing the same Co and Zr metals, the XPS valence band spectra demonstrate a significant difference in the electronic properties of the Co-containing type II and III systems (Figure 6). In the case of the Co-containing type II MOF, DOS exist

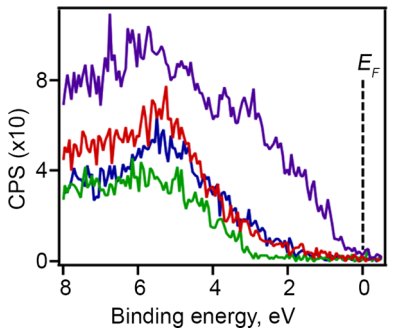

Figure 6. Valence band XPS data for: $Zr_6O_4(OH)_4$(sal-TPD)$_6$ (red), $Zr_6O_4(OH)_4$(sal-TPD-Co)$_6$ (blue), Zr_6-MOF (green), and Zr_6Co_4-MOF (purple). A sample treatment is given in Table 1.

near E_F as also observed for the bimetallic $Cu_{3-y}Co_y(BTC)_2$. In contrast, the type III MOF shows no DOS near E_F, which is similar to the insulating behavior of $Cu_{3-y}Zn_y(BTC)_2$. Notably, the type II MOF in the absence of Co also exhibits a lack of intensity in the valence band region near E_F. Therefore, these results illustrate that DOS for the Co-containing type II MOF is similar to the $Cu_{3-y}Co_y$(BTC) despite the fact that the bimetallic MOFs possess different topology, metal node geometry, and nature of the primary metal.

CONCLUSION

In this work, we studied the fundamental properties responsible for the electronic behavior of three distinct classes of bimetallic systems, $M_{x-y}M'_y$-MOFs (replacement of M by M′ in metal nodes), $M_xM'_y$-MOFs (node extension through M′ incorporation), and M_x(ligand-M'_y)-MOFs (coordination of M′ to the organic linker). We showed that, in addition to metal node engineering, the presence of unsaturated metal sites as well as framework topology can potentially affect the density of electronic states near the Fermi edge. In particular, for the example of bimetallic Zr/Co-containing frameworks (type II and III), we demonstrated that changes in the MOF electronic structure depend on the site chosen for second metal coordination (i.e., a metal node versus an organic linker). We also showed that the valence band spectra of evacuated monometallic M-MOFs (M = Cu and Zn) and bimetallic $M_{3-y}M'_y$-MOFs (M = Cu, M′ = Zn) exhibit zero intensity near the Fermi level, which is characteristic of insulators, while bimetallic cobalt-containing type-I and type-II MOFs exhibit semiconductor behavior. Microwave conductivity measurements demonstrated the correlation of the changes observed in an electronic structure and material properties. These experimental data are consistent with theoretical calculations, which indicate that the incorporation of the second metal (M′) inside the MOF matrix could result in significant changes in the DOS. In particular we found that, in the monometallic Cu-BTC system, the DOS near E_F originate mainly from the oxygen p-orbitals, and the DOS above E_F (conduction band) is composed of copper d-orbitals. However, due to cobalt incorporation into the framework matrix, the DOS near E_F is dominated by contributions from cobalt d-orbitals, and the estimated decrease in the band gap was calculated to be 0.6 eV. Thus, the presented studies begin to elucidate the key factors responsible for tunability of MOF electronic structure as a function of second metal incorporation, while preserving the main inherent property of MOFs—porosity.

EXPERIMENTAL SECTION

Materials. $Cu(NO_3)_2{\cdot}2.5H_2O$ (98.3%, Mallinckrodt AR), $Cu(OAc)_2{\cdot}H_2O$ (>95%, TCI America), $CoCl_2{\cdot}6H_2O$ (>98.0%, TCI America), $Zn(NO_3)_2{\cdot}6H_2O$ (technical grade, Ward's Science), $Co(NO_3)_2{\cdot}6H_2O$ (99%, STREM Chemicals, Inc.), $ZrCl_4$ (99.5%, Alfa Aesar), CsF (99%, Oakwood Chemical), K_2CO_3 (lab grade, Ward's Science), NaOH (ACS grade, Fisher Chemical), NaCl (ACS grade, BDH), KOH (ACS grade, Fisher Chemical), $MgSO_4$ (reagent grade, Oakwood Chemical), 1,3,5-benzenetricarboxylic acid (98%, Alfa Aesar), 1,3,5-tribromobenzene (>95%, Matrix Scientific), 4-methoxycarbonyl phenylboronic acid (>97%, Boronic Molecular), palladium(II) acetate (>95+%, Ox-Chem), polyethylene glycol 400 (lab grade, Merck Millipore), methyl 4-iodo-3-methylbenzoate (98%, BeamTown Chemical), 4,4,4′,4′,5,5,5′,5′-octamethyl-2,2′-bi(1,3,2-dioxaborolane) (>98%, Ark Pharm), bis(triphenylphosphine)palladium(II) chloride (96%, Oakwood Chemical), 2,5-dibromoaniline (97%, Oakwood Chemical), triphenylphosphine (99%, Sigma-Aldrich), 4,4′-bipyridyl (98%, Sigma-Aldrich), salicylaldehyde (99% Alfa Aesar), pyridine (99+%, Alfa Aesar), *N*,*N*′-dimethylformamide (ACS grade, BDH), methanol (>99.8%, HPLC grade, Fisher Scientific), ethyl acetate (ACS grade, Merck Millipore), hexane (ACS grade, Macron Fine Chemicals), ethanol (200 proof, Decon Laboratories, Inc.), tetrahydrofuran (ACS grade, Macron Fine Chemicals), chloroform (ACS grade, Macron Fine Chemicals), dimethyl sulfoxide (ACS grade, Fisher Scientific), dichloromethane (ACS grade, Oakwood Chemical), trifluoroacetic acid (99%, Oakwood Chemical), glacial acetic acid (ACS grade, BDH), hydrochloric acid (ACS grade, Sigma-Aldrich), chloroform-*d* (Cambridge Isotope Laboratories, Inc.), and DMSO-d_6 (Cambridge Isotope Laboratories, Inc.) were used as received.

Synthesis. The compounds $Cu_3(BTC)_2$,[66] $Zn_3(BTC)_2$,[40] $Co_6(BTC)_2(HCO_2)_6(DMF)_6$[59] ($HCO_2$ = formate), $Cu_3(BTB)_2$,[67] $Cu_6(BTB)_4(BP)_3$,[60] $Co_6(BTB)_4(BP)_3$,[60] $Zr_6O_4(OH)_8(H_2O)_4(Me_2BPDC)_4$ (Me_2BPDC = 2,2′-dimethylbiphenyl-4,4′-dicarboxylate), [Zr_6-MOF],[49] $Zr_6Co_4O_8(OH)_8(H_2O)_8(Me_2BPDC)_4$, [$Zr_6Co_4$-MOF],[49] $Zr_6O_4(OH)_4$(sal-TPD)$_6$[50] (sal-TPD = salicylaldimine terphenyl dicarboxylate), $Zr_6O_4(OH)_4$(sal-TPD-Co),[50] H_2(sal-TPD),[50] H_3BTB,[68] and H_2Me_2BPDC,[69] were prepared according to the reported procedures.

Preparation of $Cu_{3-y}Co_y(BTC)_2$ Systems. In a 20 mL vial, freshly prepared $Cu_3(BTC)_2$ (0.135 g, 0.203 mmol) and a solution of $CoCl_2$ (10 mL DMF) were heated at 90 °C for 24 h in an isothermal oven. For the preparation of $Cu_{2.82}Co_{0.18}(BTC)_2$, $Cu_{2.4}Co_{0.6}(BTC)_2$, and $Cu_{1.5}Co_{1.5}(BTC)_2$, the concentrations of $CoCl_2$ were 0.147, 0.294, and 0.441 M, respectively. After 24 h heating, the reaction mixture was cooled down to room temperature, and the resulting green powder was washed thoroughly with DMF to remove excess cobalt chloride. After DMF washing, the powder was soaked in dichloromethane at room temperature. The solvent was replaced twice a day over 72 h before further characterization.

Preparation of $Cu_{3-y}Zn_y(BTC)_2$ Systems. The crystals of $Zn_3(BTC)_2$ (1.00 g, 0.533 mmol) were soaked in 2 mL of saturated

DOI: 10.1021/jacs.7b01125
J. Am. Chem. Soc. XXXX, XXX, XXX−XXX

copper nitrate solution in ethanol (1.01 M) at room temperature. For the preparation of $Cu_{1.05}Zn_{1.95}(BTC)_2$ and $Cu_{2.25}Zn_{0.75}(BTC)_2$, the reaction time was chosen as 9 and 18 h, respectively. The resulting blue crystals were washed thoroughly with DMF to remove excess copper nitrate and stored under DMF until further characterization.

Preparation of $Cu_{6-y}Co_y(BTB)_4(BP)_3$ Systems. The $Cu_{2.34}Co_{3.66}(BTB)_4(BP)_3$ sample was synthesized by heating a mixture of H_3BTB (44.7 mg, 0.102 mmol), BP (8.90 mg, 0.0570 mmol), $Cu(NO_3)_2{\cdot}2.5H_2O$ (15.9 mg, 0.0685 mmol), and $Co(NO_3)_2{\cdot}6H_2O$ (19.9 mg, 0.0685 mmol) in 5 mL of DMF at 100 °C for 96 h. To remove an excess of the reagents, the synthesized MOF was thoroughly washed by DMF. The washing procedure was repeated three times a day with fresh DMF for 3 days.

X-ray Photoelectron Spectroscopy Studies. XPS data were collected using a Kratos AXIS Ultra DLD system equipped with a hemispherical analyzer and monochromatic Al K_α source; this vacuum system has been described in detail elsewhere.[56] The base pressure of the vacuum chamber was 2×10^{-9} Torr before sample introduction and $\leq 2 \times 10^{-8}$ Torr during experiments. A charge neutralizer was used to compensate for charging by bombarding the sample with low-energy electrons, and binding energies were set according to the position of adventitious carbon at 284.8 eV. A step size of 0.06 eV and dwell times of 600 ms for O(1s), 800 ms for C(1s), N(1s), and Cl(2p), and 1600 ms for Cu(2p), Co(2p), Zn(2p), and Zr(3d) the $Cu(L_3M_5M_5)$ region, and the valence band region were used. Survey scans were also collected to ensure there were no contaminants introduced during sample preparation. Samples could be directly transferred to a catalysis cell without exposure to air. In the catalysis cell, the samples were treated at temperatures ranging from room temperature to 225 °C under a pure gas flow of Ar (Airgas, UHP 99.999%). The samples were heated by means of a shielded boron nitride button heater, and the sample temperature was measured by a type K thermocouple pin on which the sample holder was positioned in the catalysis cell.

Microwave Conductivity Measurements. Our microwave conductivity measurements consist of observing the change in resonance characteristics induced in a microwave cavity by the sample of interest. This experiment was carried out using a custom-built microwave circuit in an X-band waveguide. A voltage-controlled oscillator (Sievers V03262X/00) provided a frequency-tunable microwave power source with an output of ∼100 mW, which was computer controlled via a programmable voltage source (Keithley 230). The sample was mounted on a fused quartz slide near one of the electric-field maxima inside a custom-built TE_{102} microwave resonator, with a natural resonance frequency of ∼8.9 GHz and a quality factor of ∼200. The power reflection coefficient from the cavity was measured as a function of microwave frequency using a Schottkey barrier diode (1N23C) mounted inside a waveguide short, the (50 ohm terminated) voltage output of which was digitized through a source-measure unit (Keithley 236). The power reflection coefficient was calculated from the detector voltage by converting voltage into microwave power using a previously determined calibration curve (acquired using a pyroelectric power meter), and taking the ratio of power reflected from the cavity to that reflected from a brass plate mounted at the same position. The interpretation of the acquired data was done through explicit electromagnetic simulations of the cavity response to sample properties, as we describe in the Supporting Information.

Inductively Coupled Plasma Atomic Emission Spectroscopy (ICP-AES). ICP-AES analysis was conducted using a Finnigan ELEMENT XR double focusing magnetic sector field inductively coupled plasma-mass spectrometer (SF-ICP-MS) with Ir and/or Rh as internal standards. A Micromist U-series nebulizer (0.2 mL/min, GE, Australia), quartz torch, and injector (Thermo Fisher Scientific, USA) were used for sample introduction. The sample gas flow was 1.08 mL/min, and the forwarding power was 1250 W. The samples were digested in Teflon vessels with nitric and hydrochloric acids and then heated at 180 °C for 4 h.

Computational Details. DFT calculations were performed using a finite size cluster model cut out from the crystallographically determined structure of $Cu_3(BTC)_2$, which contains a Cu^{2+} dimer surrounded by four BTC units with the carboxylates saturated with H atoms. The bimetallic Co−Cu−BTC model was created by replacing one of the Cu atoms with Co in our $Cu_2(BTC)_4$ cluster model which corresponds to 50% substitution of the second metal. Geometry optimizations were carried out employing the hybrid B3LYP method[70−72] (Becke's three-parameter exchange functional and the correlation functional from Lee, Yang, and Parr) and the def2-TZVPP basis set[73,74] (Ahlrichs' split-valence triple-ζ basis set with polarization functions on all atoms with additional polarization functions) using the TURBOMOLE 6.6 program package.[75] Grimme's DFT-D3 method[76] was used for including the dispersion corrections for the nonbonding van der Waals interactions and the density of states for the clusters were obtained using Gaussian smearing of the Kohn−Sham orbital energies.

Other Physical Measurements. Powder X-ray diffraction patterns were recorded on a Rigaku Miniflex II diffractometer with accelerating voltage and current of 30 kV and 15 mA, respectively. Diffuse reflectance spectra were collected from pressed pellets on a PerkinElmer Lambda 45 UV/vis spectrometer referenced to Spectralon or potassium bromide.

The conductivity on MOF pressed pellets was performed using a source meter (Keithley Instruments GmbH, Germering, Germany, model 2400). The connection between the two electrodes was established with a Signatone Mount Stand (model S-302-4) and a two-point probe (Head Inc., model SP4-62045TBY). The set up was calibrated using a VLSI Standard (100 mA, 0.011 Ohm) at 2.1 V and 100 mA.

■ ASSOCIATED CONTENT

Supporting Information

The Supporting Information is available free of charge on the ACS Publications website at DOI: 10.1021/jacs.7b01125.

MOF crystal structures, secondary building units, XPS spectra, description of assignment of cobalt oxidation states from XPS, PXRD patterns, microwave conductivity data, and diffuse reflectance data (PDF)

■ AUTHOR INFORMATION

Corresponding Authors

*CHEND@mailbox.sc.edu

*shustova@sc.edu

ORCID

Andreas Heyden: 0000-0002-4939-7489

Donna A. Chen: 0000-0003-4962-5530

Natalia B. Shustova: 0000-0003-3952-1949

Notes

The authors declare no competing financial interest.

■ ACKNOWLEDGMENTS

Acknowledgement is made to the Donors of the American Chemical Society Petroleum Research Fund for support of this research. N.B.S. gratefully acknowledges support from the NSF CAREER Award (DMR-1553634) and a Cottrell Scholar Award from the Research Corporation for Science Advancement. D.A.C. also acknowledges financial support from the NSF (CHE-300227), and A.J.B. acknowledges funding from an NSF IGERT grant (DGE-1250052). N.B.S. and D.A.C. are grateful for support from the Savannah River National Laboratory/Department of Energy Program. B.W.L. and O.G.R. thank the Solar Photochemistry Program, Division of Chemical Sciences, Geosciences, and Biosciences, Office of Basic Energy Sciences, U.S. Department of Energy under Contract DE-AC36-08-GO28308 with the National Renewable Energy Laboratory for financial support. We also acknowledge

DOI: 10.1021/jacs.7b01125
J. Am. Chem. Soc. XXXX, XXX, XXX−XXX

the University of South Carolina College of Engineering and Computing X-ray Photoelectron Spectroscopy Facility for use of the instrument. A.H. acknowledges support from the NSF (CBET-1254352). This research used resources of the National Energy Research Scientific Computing Center, a DOE Office of Science User Facility supported by the Office of Science of the U.S. Department of Energy under Contract No. DE-AC02-05CH11231.

REFERENCES

(1) Zhou, H.-C.; Long, J. R.; Yaghi, O. M. *Chem. Rev.* **2012**, *112*, 673−674.
(2) Sun, L.; Campbell, M. G.; Dincă, M. *Angew. Chem., Int. Ed.* **2016**, *55*, 3566−3579.
(3) Horike, S.; Umeyama, D.; Kitagawa, S. *Acc. Chem. Res.* **2013**, *46*, 2376−2384.
(4) Allendorf, M. D.; Schwartzberg, A.; Stavila, V.; Talin, A. A. *Chem. - Eur. J.* **2011**, *17*, 11372−11388.
(5) Zhang, T.; Lin, W. *Chem. Soc. Rev.* **2014**, *43*, 5982−5993.
(6) Zhou, H.-C.; Kitagawa, S. *Chem. Soc. Rev.* **2014**, *43*, 5415−5418.
(7) Leong, C. F.; Usov, P. M.; D'Alessandro, D. M. *MRS Bull.* **2016**, *41*, 858−864.
(8) Darago, L. E.; Aubrey, M. L.; Yu, C. J.; Gonzalez, M. I.; Long, J. R. *J. Am. Chem. Soc.* **2015**, *137*, 15703−15711.
(9) Zeng, M.-H.; Wang, Q.-X.; Tan, Y.-X.; Hu, S.; Zhao, H.-X.; Long, L.-S.; Kurmoo, M. *J. Am. Chem. Soc.* **2010**, *132*, 2561−2563.
(10) Zhai, Q.-G.; Mao, C.; Zhao, X.; Lin, Q.; Bu, F.; Chen, X.; Bu, X.; Feng, P. *Angew. Chem., Int. Ed.* **2015**, *54*, 7886−7890.
(11) Kreno, L. E.; Leong, K.; Farha, O. K.; Allendorf, M.; Van Duyne, R. P.; Hupp, J. T. *Chem. Rev.* **2012**, *112*, 1105−1125.
(12) Nouar, F.; Eubank, J. F.; Bousquet, T.; Wojtas, L.; Zaworotko, M. J.; Eddaoudi, M. *J. Am. Chem. Soc.* **2008**, *130*, 1833−1835.
(13) Gándara, F.; Uribe-Romo, F. J.; Britt, D. K.; Furukawa, H.; Lei, L.; Cheng, R.; Duan, X.; O'Keeffe, M.; Yaghi, O. M. *Chem. - Eur. J.* **2012**, *18*, 10595−10601.
(14) Choi, K. M.; Jeong, H. M.; Park, J. H.; Zhang, Y.-B.; Kang, J. K.; Yaghi, O. M. *ACS Nano* **2014**, *8*, 7451−7457.
(15) Stavila, V.; Talin, A. A.; Allendorf, M. D. *Chem. Soc. Rev.* **2014**, *43*, 5994−6010.
(16) Silva, C. G.; Corma, A.; García, H. *J. Mater. Chem.* **2010**, *20*, 3141−3156.
(17) Komatsu, T.; Taylor, J. M.; Kitagawa, H. *Inorg. Chem.* **2016**, *55*, 546−548.
(18) Takaishi, S.; Hosoda, M.; Kajiwara, T.; Miyasaka, H.; Yamashita, M.; Nakanishi, Y.; Kitagawa, Y.; Yamaguchi, K.; Kobayashi, A.; Kitagawa, H. *Inorg. Chem.* **2009**, *48*, 9048−9050.
(19) Guo, Z.; Panda, D. K.; Maity, K.; Lindsey, D.; Parker, T. G.; Albrecht-Schmitt, T. E.; Barreda-Esparza, J. L.; Xiong, P.; Zhou, W.; Saha, S. *J. Mater. Chem. C* **2016**, *4*, 894−899.
(20) Hendon, C. H.; Tiana, D.; Walsh, A. *Phys. Chem. Chem. Phys.* **2012**, *14*, 13120−13132.
(21) Campbell, M. G.; Sheberla, D.; Liu, S. F.; Swager, T. M.; Dincă, M. *Angew. Chem., Int. Ed.* **2015**, *54*, 4349−4352.
(22) Lee, Y.; Kim, S.; Kang, J. K.; Cohen, S. M. *Chem. Commun.* **2015**, *51*, 5735−5738.
(23) Wang, L.; Han, Y.; Feng, X.; Zhou, J.; Qi, P.; Wang, B. *Coord. Chem. Rev.* **2016**, *307*, 361−381.
(24) Talin, A. A.; Centrone, A.; Ford, A. C.; Foster, M. E.; Stavila, V.; Haney, P.; Kinney, R. A.; Szalai, V.; El Gabaly, F.; Yoon, H. P.; Léonard, F.; Allendorf, M. D. *Science* **2014**, *343*, 66−68.
(25) Narayan, T. C.; Miyakai, T.; Seki, S.; Dincă, M. *J. Am. Chem. Soc.* **2012**, *134*, 12932−12935.
(26) Zhang, Z.; Awaga, K. *MRS Bull.* **2016**, *41*, 883−889.
(27) Park, S. S.; Hontz, E. R.; Sun, L.; Hendon, C. H.; Walsh, A.; Van Voorhis, T.; Dincă, M. *J. Am. Chem. Soc.* **2015**, *137*, 1774−1777.
(28) Liu, D.; Lu, K.; Poon, C.; Lin, W. *Inorg. Chem.* **2014**, *53*, 1916−1924.
(29) Lu, G.; Hupp, J. T. *J. Am. Chem. Soc.* **2010**, *132*, 7832−7833.
(30) Sun, L.; Hendon, C. H.; Minier, M. A.; Walsh, A.; Dincă, M. *J. Am. Chem. Soc.* **2015**, *137*, 6164−6167.
(31) Díaz, R.; Orcajo, M. G.; Botas, J. A.; Calleja, G.; Palma, J. *Mater. Lett.* **2012**, *68*, 126−128.
(32) Huang, Z.-F.; Song, J.; Li, K.; Tahir, M.; Wang, Y.-T.; Pan, L.; Wang, L.; Zhang, X.; Zou, J.-J. *J. Am. Chem. Soc.* **2016**, *138*, 1359−1365.
(33) Wu, G.; Huang, J.; Zang, Y.; He, J.; Xu, G. *J. Am. Chem. Soc.* **2017**, *139*, 1360−1363.
(34) Kim, M.; Cahill, J. F.; Fei, H.; Prather, K. A.; Cohen, S. M. *J. Am. Chem. Soc.* **2012**, *134*, 18082−18088.
(35) Deria, P.; Mondloch, J. E.; Karagiaridi, O.; Bury, W.; Hupp, J. T.; Farha, O. K. *Chem. Soc. Rev.* **2014**, *43*, 5896−5912.
(36) Lalonde, M.; Bury, W.; Karagiaridi, O.; Brown, Z.; Hupp, J. T.; Farha, O. K. *J. Mater. Chem. A* **2013**, *1*, 5453−5468.
(37) Zhai, Q.-G.; Bu, X.; Mao, C.; Zhao, X.; Feng, P. *J. Am. Chem. Soc.* **2016**, *138*, 2524−2527.
(38) Zhang, Z.; Zhang, L.; Wojtas, L.; Nugent, P.; Eddaoudi, M.; Zaworotko, M. J. *J. Am. Chem. Soc.* **2012**, *134*, 924−927.
(39) Brozek, C. K.; Dincă, M. *Chem. Soc. Rev.* **2014**, *43*, 5456−5467.
(40) Song, X.; Jeong, S.; Kim, D.; Lah, M. S. *CrystEngComm* **2012**, *14*, 5753−5756.
(41) Cohen, S. M. *J. Am. Chem. Soc.* **2017**, *139*, 2855−2863.
(42) Sun, L.; Park, S. S.; Sheberla, D.; Dincă, M. *J. Am. Chem. Soc.* **2016**, *138*, 14772−14782.
(43) Li, H.; Eddaoudi, M.; O'Keeffe, M.; Yaghi, O. M. *Nature* **1999**, *402*, 276−279.
(44) Choi, J. H.; Choi, Y. J.; Lee, J. W.; Shin, W. H.; Kang, J. K. *Phys. Chem. Chem. Phys.* **2009**, *11*, 628−631.
(45) Brozek, C. K.; Dincă, M. *J. Am. Chem. Soc.* **2013**, *135*, 12886−12891.
(46) Kaye, S. S.; Dailly, A.; Yaghi, O. M.; Long, J. R. *J. Am. Chem. Soc.* **2007**, *129*, 14176−14177.
(47) Brozek, C. K.; Michaelis, V. K.; Ong, T.-C.; Bellarosa, L.; López, N.; Griffin, R. G.; Dincă, M. *ACS Cent. Sci.* **2015**, *1*, 252−260.
(48) Zhang, S.-Y.; Li, D.; Guo, D.; Zhang, H.; Shi, W.; Cheng, P.; Wojtas, L.; Zaworotko, M. J. *J. Am. Chem. Soc.* **2015**, *137*, 15406−15409.
(49) Yuan, S.; Chen, Y.-P.; Qin, J.; Lu, W.; Wang, X.; Zhang, Q.; Bosch, M.; Liu, T.-F.; Lian, X.; Zhou, H.-C. *Angew. Chem., Int. Ed.* **2015**, *54*, 14696−14700.
(50) Manna, K.; Zhang, T.; Carboni, M.; Abney, C. W.; Lin, W. *J. Am. Chem. Soc.* **2014**, *136*, 13182−13185.
(51) Jee, B.; Eisinger, K.; Gul-E-Noor, F.; Bertmer, M.; Hartmann, M.; Himsl, D.; Pöppl, A. *J. Phys. Chem. C* **2010**, *114*, 16630−16639.
(52) Gul-E-Noor, F.; Jee, B.; Mendt, M.; Himsl, D.; Pöppl, A.; Hartmann, M.; Haase, J.; Krautscheid, H.; Bertmer, M. *J. Phys. Chem. C* **2012**, *116*, 20866−20873.
(53) Gotthardt, M. A.; Schoch, R.; Wolf, S.; Bauer, M.; Kleist, W. *Dalton. Trans.* **2015**, *44*, 2052−2056.
(54) Parkes, M. V.; Sava Gallis, D. F.; Greathouse, J. A.; Nenoff, T. M. *J. Phys. Chem. C* **2015**, *119*, 6556−6567.
(55) Sahiner, N.; Demirci, S.; Yildiz, M. *J. Electron. Mater.* **2017**, *46*, 790−801.
(56) Duke, A. S.; Dolgopolova, E. A.; Galhenage, R. P.; Ammal, S. C.; Heyden, A.; Smith, M. D.; Chen, D. A.; Shustova, N. B. *J. Phys. Chem. C* **2015**, *119*, 27457−27466.
(57) Liu, J.; Zhu, R.; Xu, T.; Xu, Y.; Ge, F.; Xi, Y.; Zhu, J.; He, H. *Chemosphere* **2016**, *144*, 1148−1155.
(58) Wagner, C. D.; Riggs, W. M.; Davis, L. E.; Moulder, J. F. *Handbook of X-Ray Photoelectron Spectroscopy*; Perkin Elmer Corporation: Eden Prairie, MN, 1979.
(59) He, J.; Zhang, Y.; Pan, Q.; Yu, J.; Ding, H.; Xu, R. *Microporous Mesoporous Mater.* **2006**, *90*, 145−152.
(60) Song, X.; Kim, T. K.; Kim, H.; Kim, D.; Jeong, S.; Moon, H. R.; Lah, M. S. *Chem. Mater.* **2012**, *24*, 3065−3073.
(61) Nasalevich, M. A.; Goesten, M. G.; Savenije, T. J.; Kapteijn, F.; Gascon, J. *Chem. Commun.* **2013**, *49*, 10575−10577.

DOI: 10.1021/jacs.7b01125
J. Am. Chem. Soc. XXXX, XXX, XXX−XXX

(62) Sun, L.; Miyakai, T.; Seki, S.; Dincă, M. *J. Am. Chem. Soc.* **2013**, *135*, 8185−8188.
(63) Grozema, F. C.; Siebbeles, L. D. A.; Warman, J. M.; Seki, S.; Tagawa, S.; Scherf, U. *Adv. Mater.* **2002**, *14*, 228−231.
(64) Usman, M.; Mendiratta, S.; Batjargal, S.; Haider, G.; Hayashi, M.; Rao Gade, N.; Chen, J.-W.; Chen, Y.-F.; Lu, K.-L. *ACS Appl. Mater. Interfaces* **2015**, *7*, 22767−22774.
(65) López, R.; Gómez, R. *J. Sol-Gel Sci. Technol.* **2012**, *61*, 1−7.
(66) Liu, J.; Wang, Y.; Benin, A. I.; Jakubczak, P.; Willis, R. R.; LeVan, M. D. *Langmuir* **2010**, *26*, 14301−14307.
(67) Chen, B.; Eddaoudi, M.; Hyde, S. T.; O'Keeffe, M.; Yaghi, O. M. *Science* **2001**, *291*, 1021−1023.
(68) Bednaříková, T.; Tošner, Z.; Horský, J.; Jindřich, J. *J. Inclusion Phenom. Macrocyclic Chem.* **2015**, *81*, 141−152.
(69) Burrows, A. D.; Frost, C. G.; Mahon, M. F.; Richardson, C. *Chem. Commun.* **2009**, 4218−4220.
(70) Becke, A. D. *Phys. Rev. A: At., Mol., Opt. Phys.* **1988**, *38*, 3098−3100.
(71) Becke, A. D. *J. Chem. Phys.* **1993**, *98*, 5648−5652.
(72) Lee, C.; Yang, W.; Parr, R. G. *Phys. Rev. B: Condens. Matter Mater. Phys.* **1988**, *37*, 785−789.
(73) Schäfer, A.; Huber, C.; Ahlrichs, R. *J. Chem. Phys.* **1994**, *100*, 5829−5835.
(74) Weigend, F.; Ahlrichs, R. *Phys. Chem. Chem. Phys.* **2005**, *7*, 3297−3305.
(75) *Turbomole V6.6 2014*, a development of University of Karlsruhe and Forschungszentrum Karlsruhe GmbH, 1989−2007, TURBOMOLE GmbH; available from http://www.turbomole.com.
(76) Grimme, S.; Antony, J.; Ehrlich, S.; Krieg, H. *J. Chem. Phys.* **2010**, *132*, 154104−154122.

DOI: 10.1021/jacs.7b01125
J. Am. Chem. Soc. XXXX, XXX, XXX−XXX